Applied Catalysis B: Environmental 284 (2021) 119711

Contents lists available at ScienceDirect

Applied Catalysis B: Environmental

journal homepage: www.elsevier.com/locate/apcatb

# Designing perovskite catalysts for controlled active-site exsolution in the microwave dry reforming of methane

Chris M. Marin [a,b,*], Eric J. Popczun [a,b], Thuy-Duong Nguyen-Phan [a,b], De Nyago Tafen [a,c], Dominic Alfonso [a], Iradwikanari Waluyo [d], Adrian Hunt [d], Douglas R. Kauffman [a,*]

[a] National Energy Technology Laboratory, 626 Cochrans Mill Rd, Pittsburgh, PA, 15236, USA
[b] Leidos Research Support Team, 626 Cochrans Mill Rd, Pittsburgh, PA, 15236, USA
[c] Leidos Research Support Team, 1450 Queen Avenue SW, Albany, OR, 97321, USA
[d] Photon Sciences Division, National Synchrotron Light Source II, Brookhaven National Laboratory, Upton, NY, 11973, USA

ARTICLE INFO

*Keywords:*
Dry reforming of methane
Microwave
In situ XRD
Perovskite
Lanthanum strontium cobaltite

ABSTRACT

The dry reforming of methane (DRM) is a promising process for generating syngas (CO + $H_2$) while consuming $CO_2$, but industrial applications have been limited due to the high temperatures required to prevent coke formation. Microwave-assisted DRM (MW-DRM) is a promising approach to enable high temperature reactions because it can utilize excess renewable electrons to rapidly and selectively heat the catalyst bed without wasting time and energy heating the entire reactor. Here we demonstrate the MW-DRM reaction by modifying lanthanum strontium cobaltite (LSC) to serve as both microwave absorber and catalyst. Catalyst doping studies revealed the addition of oxophilic transition metals prevented over-reduction and stabilized the perovskitic phases under reaction conditions. In situ, synchrotron-based x-ray diffraction revealed the catalyst becomes active once metallic cobalt forms on a retained perovskitic support. The best performing Mn doped LSC catalyst showed 80–90 % single-pass conversions, stable operation for over 10 h, and easy microwave regeneration.

## 1. Introduction

$CO_2$ and $CH_4$ are both considered greenhouse gases implicated in climate change [1]. Carbon dioxide emissions from fossil fuel-based energy production have long been a point of concern. However, methane is an even stronger greenhouse gas, and is of growing concern and declining cost due to it making up a large component of shale gas [2], and it is frequently flared off at gas wells due to methane not being valuable enough to transport. Potential future fuel sources, such as gas hydrates, are expected to generate an even larger ratio of methane relative to other hydrocarbons [3]. Unfortunately, both $CO_2$ and $CH_4$ are challenging chemical feedstocks due to their molecular stability, poor reaction kinetics, and thermodynamics that generally favor methane overoxidation to $CO_2$ [4].

One potential way to utilize both $CO_2$ and $CH_4$ is by the dry reforming of methane reaction (DRM). In this reaction, $CO_2$ and methane are reacted over a catalyst to generate CO and $H_2$ (syngas) in a 1:1 ratio that is suitable for gas-to-liquids processing into longer-chain hydrocarbons or aromatics *via* the Fischer-Tropsch reaction [5]. However, commercialization of the dry reforming reaction has been limited due to the high temperatures required to drive the reaction and prevent coke formation [6], and industrial DRM demonstrations have generally been limited to niche applications such as in the direct reduction of iron [7], although dry reforming is starting to be explored for commercial scale up [8].

Microwave systems are a potential enabler for high temperature reactions because they can selectively and efficiently heat the catalyst bed without needing to heat the entire reactor volume [9,10]. From a functional perspective, the catalyst bed can be kept hundreds of degrees hotter than the surroundings and the necessary energy is efficiently directed to where the chemistry occurs: at the surface of the heterogeneous catalyst. Direct microwave heating of the catalyst itself has the additional benefit of greatly reducing the thermal mass of the system, allowing for rapid heat up and cool down times compared to a conventional thermal reactor. This contrasts with conventional indirect heating methods where the temperature of the heat source must be considerably above the catalyst temperature and in which heat transport to the catalyst determines the startup and cooldown rates [11]. The

* Corresponding authors at: National Energy Technology Laboratory, 626 Cochrans Mill Rd, Pittsburgh, PA, 15236, USA.
*E-mail addresses:* Christopher.Marin@netl.doe.gov (C.M. Marin), Douglas.Kauffman@netl.doe.gov (D.R. Kauffman).

https://doi.org/10.1016/j.apcatb.2020.119711
Received 23 June 2020; Received in revised form 5 October 2020; Accepted 27 October 2020
Available online 25 November 2020

rapid and selective microwave heating of the catalyst bed suggests this approach could efficiently couple with excess or intermittent renewable electricity for on-demand production of carbon neutral chemicals.

The temperatures achieved from microwave energy are a function of both the applied power and the material's microwave absorptivity (susceptibility). Desirable MW-DRM catalysts must be designed for both chemical selectivity and efficient microwave absorption, and this added complexity has limited their application as most oxide materials used as catalyst supports (e.g. $SiO_2$, $TiO_2$, $Al_2O_3$, etc.) are not good absorbers. Microwave absorptivity is largely determined by the loss tangent (tanδ) of the material, defined as:

$$\tan\delta = (\omega\varepsilon'' + \sigma)/\omega\varepsilon'$$

where ω is the angular frequency of the wave, ε'' is the imaginary component of permittivity, ε' is the lossless (real) permittivity, and σ is the free charge conduction of the material. One approach for improving microwave absorptivity is to maximize the material's conductivity. Pure metal powders have good conductivities, but they are generally poor MW catalysts because they can sinter under reducing conditions and become non-conducting oxides under oxidizing conditions. Activated carbon is a commonly used microwave absorber that has been heavily explored for MW-DRM applications [10,12], but coke formation below 1173 K [6], carbon pyrolysis above 1173 K [10], and an inability to regenerate the catalyst under oxidizing conditions limit its potential as a suitable MW-DRM catalyst.

A desirable inorganic MW-DRM catalyst should maintain excellent conductivity at high temperatures, demonstrate stability under both reducing and oxidizing conditions (for ease of regeneration), and readily adsorb and activate both $CO_2$ and $CH_4$. Traditional thermal DRM catalysts often contain a metal center for methane adsorption and dissociation, and a basic oxide support to adsorb acidic $CO_2$ molecules and weaken the strong $CO_2$ double bonds. Catalyst examples include Ni, Co, Fe, Pt, Rh, Ru, Ir, or Pd particles [13–18] supported on irreducible oxides, such as $SiO_2$, $Al_2O_3$, $TiO_2$, $CeO_2$, and $La_2O_3$.Basic promoters, such as $Ca^{2+}$, $Mg^{2+}$, $Y^{3+}$, or $La^{3+}$ also aid in $CO_2$ adsorption and assist in coke oxidation [13]. However, oxides such as $SiO_2$ and $La_2O_3$ are non-conductive and poor microwave absorbers that require high metal loadings (~10 %) to create sufficiently large loss tangents for MW heating, and only then if they are pre-reduced in a thermal reactor under hydrogen so that the catalyst is metallic and conductive. For instance, excellent MW-DRM performance has been demonstrated for high platinum loadings on alumina catalysts (8% Pt: $Al_2O_3$) when pre-reduced in $H_2$ with $CH_4$ and $CO_2$ conversions between 90–95 % at 130 W of applied MW power [19]. Additionally, transition metals such as cobalt have been explored as an alternative to platinum group metals with $Al_2O_3$--supported Co-Mo alloys demonstrating 80 % $CH_4$ conversion and 93 % $CO_2$ conversion at 200 W while producing $H_2$ and CO at a 0.8:1 ratio [20]. In both cases, oxidative conditions (such as when combusting off coke) will cause the conductive metal to oxidize and necessitates re-reduction in a thermal system with hydrogen as the oxides are non-conductive.

Recently, perovskites such ruthenium doped strontium titanate (7% Ru:$SrTiO_3$) have been explored as promising MW-DRM catalysts [21]. Perovskites are a class of oxides taking the form of $ABO_3$ where A is generally an alkaline earth or rare earth element cation and B is a transition metal. The use of Ru doped $SrTiO_3$ allowed the in situ formation of metallic Ru nanoparticles during the calcination step even without hydrogen reduction. However, high ruthenium loadings are undesirable for large-scale applications because it is an extremely low abundance and expensive platinum group element.

Strontium doped lanthanum cobaltite ($La_xSr_{1-x}CoO_3$) is a promising perovskite-based MW-DRM catalyst candidate because it has one of the highest conductivities among oxides at 4400 S/cm [22], it can exsolve cobalt particles under high temperature reaction conditions [23], it contains no platinum group elements, and it has a high melting point of ~1700 °C. Recently, it has been found that exsolved metal nanoparticles serve as excellent active sites with strong support interactions with the remaining oxide support and are readily redissolvable back into the perovskite lattice upon heating under oxidizing conditions [24,25]. In fact, perovskite-based catalysts containing exsolved metal can be fully regenerated, and coke formations can be removed by simply heating in air, resulting in a return to the fresh parent perovskite oxide [25], a very desirable property for a dry reforming catalyst. However, the strength of the metal support interaction must be adjusted to the right level to achieve highly dispersed metal sites, yet not so high as to be non-reducible under reaction conditions [8]. The use of transition metal dopants such as Fe in $LaNiO_3$ perovskites has recently been explored as a method of controlling nanoparticle exsolution in thermally run dry reforming reactions [26,27]. This control is particularly important for microwave systems as the catalyst must serve double duty as the microwave absorber and phase changes can result in dramatically different conductivities and resulting loss tangents.

Here we report the synthesis and activity of a family of transition metal doped $La_{0.8}Sr_{0.2}CoO_3$ (LSC) based perovskite catalysts for MW-DRM. In our case, the use of transition metal dopants allowed us to rationally tune the catalyst oxophilicity, which controlled the strength of the exsolved metal-support interactions and allowed us to maximize MW-DRM performance. More oxophilic dopants increased the stability and activity for MW-DRM, whereas less oxophilic dopants lead to near complete phase segregation and severe catalyst deactivation. X-ray absorption spectroscopy (XAS) and density functional theory (DFT) were used to understand dopant-induced changes to the electronic structure of the parent LSC material. Ex situ X-ray diffraction (XRD), scanning electron microscopy (SEM), scanning transmission electron microscopy (STEM), and energy dispersive X-ray spectroscopy (EDX) were utilized to track phase changes in LSC structure as the catalysts became activated for dry reforming under reaction conditions. In situ synchrotron-based XRD (s-XRD) was used to monitor real time phase changes and identify the emergence of Co nanoparticles during the dry reforming reaction. Crucially we found that the perovskite is not just a precursor to form metal particles on a simple $La_2O_3$ support, but instead the perovskite reduced in steps with an onset of activity once Co particles formed on a retained perovskitic support. The retention of a MW-absorbing perovskitic support is essential for sustaining microwave activity as it meant that temperature and catalytic activity stayed stable rather than decreasing as the conductive perovskite support transformed to non-microwave absorbing $La_2O_3$. Understanding the effect of dopants on the activation and stability of LSC allow us to rationally formulate LSC-based microwave absorbing catalysts capable of 80–90 % single-pass $CO_2$ and $CH_4$ conversions at 90 W applied MW power, stability for over 10 h of operation, regenerability in the same microwave reactor under $CO_2$ or air, and with demonstrated conversions up to 24 $Lg^{-1}hr^{-1}$.

## 2. Experimental

### 2.1. Catalyst preparation

$La_{0.8}Sr_{0.2}Co_{0.9}M_{0.1}O_3$ perovskite synthesis was conducted using a conventional thermal method and described in detail elsewhere [28]. Briefly, stoichiometric amounts of strontium (II) carbonate [$SrCO_3$, 99.9 %, Sigma-Aldrich], lanthanum (III) oxide [$La_2O_3$, 99.5 %, Alfa-Aesar] and cobalt (II,III) oxide [$Co_3O_4$, 99 %, Sigma-Aldrich] were mixed with B-site dopants including, nickel (II) oxide [NiO, 98 % Sigma-Aldrich], iron (III) oxide [$Fe_2O_3$, 99.9 %, Alfa-Aesar], manganese (III) oxide [$Mn_2O_3$, 99 % Alfa-Aesar], or copper (I) oxide [$Cu_2O$, 98 %, Alfa-Aesar]. Mixtures were ground in an agate mortar for approx. 10−15 min. until homogenized, added to a 13 mm pellet die assembly, and pressed into pellets by applying a pressure of 4 metric tons for 15 min using a Carver, Inc. Pellet Press (#4350. L). Pellets were removed from the die assembly and heated to 1100 °C at a rate of 1.5 °C/min and held for 64 h in an alumina crucible in air at ambient pressure. Upon

completion, the sample was cooled in air to room temperature and ground into a black powder with a mortar and pestle for later use. Powder diffraction patterns for the synthesized samples were collected on a PANalytical X'Pert Pro diffractometer in order to confirm phase purity. Scans were performed from 5 to 80 degrees 2-theta with a step size of 0.016° and a scan speed of 400 s per degree.

### 2.2. Microwave catalysis

Microwave catalysis was tested using a custom-built reactor housed inside of a single mode microwave (CEM Discover SP) (Fig. S1). 350 mg of catalyst was loaded onto a quartz wool plug inside of a 1.1 cm ID quartz tube. The catalyst was tapped smooth to produce a loosely formed bed with a thickness of approximately 0.2 cm. The catalyst loaded quartz tube was then centered in a quartz round bottom flask in the microwave cavity, and gas flow was directed from the top of the quartz tube, passed through the catalyst bed, and back out the top. The top of the reaction tube was fitted with a sapphire optical window (Edmund Optics) and the catalyst bed temperature was measured with an IR pyrometer (Process Sensors SSSL-3MH1-CF4). The pyrometer was focused on 0.5 cm diameter (~0.2 $cm^2$) spot on the center of the catalyst bed to measure the average top surface temperature. In-line product analysis was conducting via mass spectrometry using a residual gas analysis system (Pfeiffer Vacuum, OmniStar), and the outlet gas was passed through a water bubbler to keep the system pressure at ~1 atm and isolated from air. For testing MW-DRM activity versus MW wattage, a gas mixture of 4% $CO_2$ and 4% $CH_4$ in nitrogen was introduced into the system shown in Fig. S1 at a 50 sccm flow rate. Dilute gases were used in these studies to slow down catalyst transitions and activation steps within the MW-DRM mechanism. Gases were initially flowed for at least 30 min until oxygen removal was verified by in-line mass spectrometry. Product formation rates were quantified with gas chromatography (GC) by collecting products into a Tedlar gas tight bag and manually injected into a Perkin Elmer Clarus 600 GC with gas tight syringes (Vici Valco). The GC was equipped with a ShinCarbon ST (Restek) packed column, TCD and FID detectors for $H_2$ and CO analysis, and the GC was calibrated using a calibration gas mixture. The microwave was then set to a delivered output of 20 W through 90 W for at least 15 min per step to ensure stable temperature and RGA gas composition sampled. The last step of each method was run for at least 20 min with the product gas from the final 10 min analyzed by GC. Experiments with undiluted gases used 0.5−1 g of catalyst, a 50:50 pre-mixed cylinder of $CO_2$ with $CH_4$ (Butler Gas), and a condenser to capture $H_2O$ vapor side-products formed at low reaction temperatures. Gas flow was started at a rate of 50 sccm with 60 W power. Power was increased in 20 W intervals to achieve >90 % conversions at each space velocity, and then the gas flow rate doubled and the power was again adjusted until reaching a maximum space velocity of ~24 $Lg^{-1}hr^{-1}$.

### 2.3. Thermal catalysis

Thermal catalysis was performed using a commercial temperature programmed gas analysis system (Micromeritics AutoChem 2950 HP) equipped with an in-line mass spectrometer (Pfeiffer Vacuum). 350 mg of catalyst was loaded onto the top of a quartz wool bed inside of a quartz U-tube. A thin top plug of quartz wool was placed on top of the loose catalyst bed with a thermocouple used for measuring the temperature at the top of the catalyst bed. Reaction gas was 4% $CO_2$, 4% $CH_4$ with a balance of $N_2$ (Butler Gas). Samples were ramped from room temperature to 1000 °C at a rate of 5 °C/min with gas composition analyzed continuously. After reaction, catalyst samples were analyzed by XRD, SEM-EDX, and STEM.

### 2.4. In situ XRD

In situ synchrotron X-ray diffraction (s-XRD) experiments were carried out at the Advanced Photon Source (APS) beamline 17-BM-B, Argonne National Laboratory. A quartz micro-capillary tube was packed with quartz wool and ~1 cm thick loose packed plug of catalyst with a thermocouple placed adjacent to the downstream end of the plug. The reactant gas stream was a pure mixture of 4 sccm $CO_2$ and 4 sccm $CH_4$. The catalyst was continuously heated at 20 °C/min from room temperature to 400 °C, and then heated at a slower rate of 10 °C/min between 400–900 °C. The catalyst was held for 10 min at 900 °C before being allowed to cool back to room temperature. Experimental limitations with the nichrome heating element prevented operating the reactor above 900 °C. Reaction products in the gas stream were measured using in-line mass spectrometry with a Pfeiffer PrismaPlus QMG 220. S-XRD measurements were collected during heating and cooling cycles using an X-ray wavelength of 0.24136 Å and a PerkinElmer amorphous silica area detector at a diffraction distance of 0.7 m. Image acquisition lasted 10 s with the shutter closed to recover the detector for 50 s for an overall s-XRD acquisition rate of 1 scan/min. Gathered image data was integrated using GSAS-II to a 2-theta vs intensity format [29].

### 2.5. X-ray absorption

Oxygen K-edge soft X-ray absorption spectroscopy (s-XAS) was performed at beamline 23-ID-2 (IOS) at National Synchrotron Light Source-II (NSLS-II) of Brookhaven National Laboratory. Powder samples were mounted on the sample holder with carbon tape and loaded into the analysis ultra-high vacuum chamber. Oxygen K-edge spectra were collected using total electron yield (TEY) detection mode by measuring the drain current of the sample. The spectra were normalized and analyzed using the Athena module of IFEFFIT software package [30].

### 2.6. Electron microscopy

Scanning electron microscopy (SEM) was performed using an FEI Quanta 600 F SEM equipped with an Oxford Inca X-act detector for energy-dispersive X-ray spectroscopy (EDX) characterization. Surface EDX maps were performed using a 10 kV beam to minimize electron penetration with a total acquisition time per scan of 1800s. Scanning transmission electron microscopy (STEM-EDX) characterization was performed using an FEI Titan Themis G2 200. STEM samples were prepared using dilute solutions of catalyst sonicated in methanol and were drop cast onto holey carbon coated copper TEM grids and allowed to air dry overnight.

### 2.7. Computational

First-principles simulations were performed using VASP 5.4 code [31] within the augmented-wave approach and with exchange-correlation effects described by the generalized gradient approximation density functional of Perdew, Burke, and Ernzerhof (PBE) [32]. The LSC and LSC-M electronic structures were modeled with spin-polarized DFT + U theory to account for the on-site Coulomb interactions of localized electrons of transition metals. The U parameters used in this work were fitted from oxide formation enthalpy by Wang et al. [33]. The U values used were 3.3, 3.9, 4.0, 4.0, and 6.0 for Co, Mn, Fe, Cu, and Ni, respectively. The LSC system was modeled using a 3 × 1 × 1 rhombohedrally distorted perovskite structure (R-3c) consisting of 90 atoms. $La_{0.8}Sr_{0.2}Co_{0.9}M_{0.1}O_3$ was modeled by substituting 2 Co with 2 M atoms (M = Fe, Mn, Cu, Ni) in the 90 atom supercell of LSC. We used 2 × 6 × 2 Monkhorst-Pack grids where we set a 500 eV cutoff for the energy. For all compositions, optimized structures were obtained by relaxing both the ion positions and cell volume until the total force on each atom was less than 0.03 eV/Å. Topological analysis of the electron density was determined using the Bader approach.

## 3. Results and discussion

### 3.1. Phase stability of LSC under MW-DRM

The scheme in Fig. 1A shows that LSC crystallizes as a rhombohedrally distorted perovskite structure (space group R-3c). Like any perovskite structure, the crystal takes the general form $ABO_3$, where A and B are cations. The A site is typically an alkaline or rare earth element, the B site is generally a transition metal, and the cations adopt a total charge of +6. The LSC structure is maintained by a network of B—O—B bonds formed by the vertex sharing of oxygen octahedra coordinated around the B site metals with A-site atoms found in the resulting holes. Under reducing conditions, LSC goes through a series of known phase changes as the fully oxidized perovskite releases oxygen [34]. Initially, the release of oxygen generates perovskitic Ruddlesden-Popper ($A_{n+1}B_nO_{3n+1}$) and periclase cobalt oxide (BO) phases (Fig. 1A, 1st reduction). Although not a true perovskite, the Ruddlesden-Popper phase maintains a layered network of B—O – B bonds. The $LaSrCoO_4$ Ruddlesden-Popper phase is reported to maintain a considerable conductivity of ~100 S/cm [35] and is expected to remain an effective microwave absorber. Further reduction forms metallic Co from the periclase phase (Fig. 1A, 2nd reduction). Additional reduction results in the separation of the perovskitic Ruddlesden-Popper phase into additional Co and microwave-inactive lanthanum and strontium oxides (shown as $A_2O_3$ in Fig. 1A, Over Reduced). This final mixture of phase separated oxides was found to heat poorly under microwave radiation, and the loss of microwave absorbing perovskitic phases limited the maximum temperature effectively achievable by pure LSC under reducing dry reforming conditions.

LSC demonstrated these phase transitions during MW-DRM reactions performed using the reactor shown in Fig. S1. LSC displays an initial self-activation step [36,37] within the first 15 min of microwave heating under $CO_2$ and $CH_4$, and no separate pre-treatment steps were required. This can be readily observed by the rapid and erratic heating (briefly spiking to ~1000 °C at 11 min into the run shown in Fig. 1B), $CH_4$ consumption, and generation of $CO_2$ (and $H_2O$) that are all consistent with methane combustion using lattice oxygen as the perovskite was reduced. Ex situ XRD during this activation period (Fig. 1C, 5 min. MW-DRM) indicated reduction of the LSC perovskite phase into Ruddlesden-Popper ($A_2BO_4$) and periclase (CoO) phases.

The catalyst temperature stabilized after approximately 15 min and the onset of MW-DRM was evidenced by the consumption of both $CH_4$ and $CO_2$ (Fig. 1B). After this initial activation, the catalyst could be cooled to ambient temperature and brought straight back to reaction

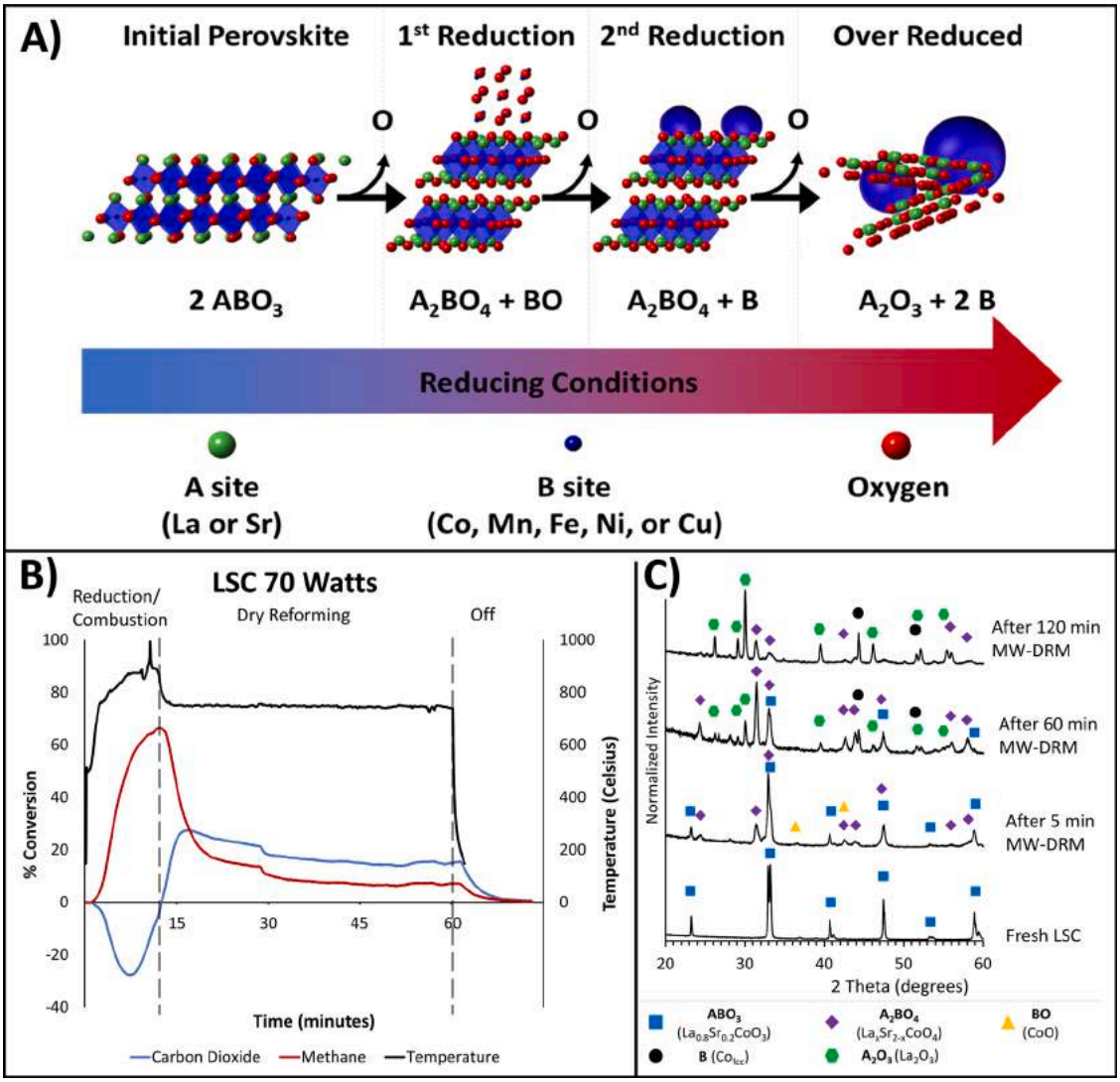


**Fig. 1.** LSC structure changes. (A) Scheme showing known phase changes upon reduction of the initial rhombohedral perovskite structure. [49] (B) Apparent temperature measured by pyrometer (black), $CO_2$ conversion (blue) and $CH_4$ conversion (red) versus time during MW-DRM at a constant 70 W power. (C) Ex situ XRD patterns taken of LSC after various MW-DRM reaction times at 70 W applied power.

temperature without requiring further activation periods if the system was not exposed to air. Cycling between on and off states, the microwave catalyst could be rapidly cycled between 150 and 700 °C with heating and cooling rates at 100−300 °C/min (Fig. S2). Ex situ XRD during steady state MW-DRM (Fig. 1C, 60 min. MW-DRM) identified a mixture of the perovskitic LSC ($ABO_3$), Ruddlesden-Popper ($A_2BO_4$), $La_2O_3$, $Co_{fcc}$, and minor $SrCO_3$ phases in the active catalysts. Despite stable temperatures, $CO_2$ and $CH_4$ conversions were below 20 % and gradually decreased with reaction time (Fig. 1B). We observed a gradual decrease in perovskitic phases with reaction time and a buildup of separated $La_2O_3$ and Co (Fig. 1C, 120 min. MW-DRM). Increasing the microwave power did not further increase temperature or conversions for LSC (Fig. 2 black points) but was found to accelerate the phase separations. Varying the concentration of strontium on the A site had no significant effect on catalytic performance for LSC (Fig. S3).

### 3.2. LSC performance with B site dopants

As the overall LSC structure is maintained by the network of B—O—B bonds, we expect that introducing more oxophilic dopant atoms into the B site can reduce oxygen release and sustain the perovskitic catalyst structure at higher temperatures. To understand the role of the LSC-dopants, we fixed the strontium A site composition at 20 % and substituted the B site at fixed 10 % loadings. Transition metals decrease in oxophilicity across a period [38], so we prepared a range of LSC-M catalysts with transition metal dopants for a composition of $La_{0.8}Sr_{0.2}Co_{0.9}M_{0.1}O_3$ where M = Mn, Fe, Co, Ni, or Cu. All LSC-M catalysts took the same initial perovskite structure (Fig. S4), which was expected due to their similarity in ionic radii and low elemental loading.

Despite their structural similarity, the prepared doped LSC catalysts demonstrated dramatically different MW-DRM performance (Fig. 2). For these tests, a fresh catalyst was loaded before each run with wattages varied from 20 to 90 W in 10 W increments under a 50 sccm flow of 4% $CO_2$ and 4% $CH_4$. As seen in Fig. 2a, all catalysts showed MW heating, with Fe and Mn dopants increasing the maximum achievable apparent temperature at high wattages. The reported apparent temperatures represent an optically-measured, surface average over a ~0.2 $cm^2$ area at the top of the catalyst bed, and we acknowledge that localized hot-spots formed during microwave heating may be hotter than the optically-measured average apparent temperature [39]. However, the trend of higher apparent temperatures with more oxophilic dopants was consistent. A short self-activation period occurred at each wattage as the perovskite became further reduced at higher temperatures. At least 15 min were given at each wattage until stable temperature and DRM product concentrations were observed, with Fig. 2 showing the steady state temperature and conversion values at each wattage. Specifically, LSC, LSC-Cu and LSC-Ni were unable to maintain apparent temperatures above ~700 °C, whereas the addition of Fe or Mn enabled higher temperatures compared with pure LSC (Fig. 2A). Despite not achieving meaningfully higher temperatures, LSC-Ni did achieve higher conversions of $CO_2$ and $CH_4$, likely due to the higher catalytic activity of Ni and Co-Ni catalysts for dry reforming relative to Co [40].

LSC-Mn demonstrated the highest MW-DRM conversions (Fig. 2B and 2) despite apparent temperatures similar to LSC-Fe. LSC-Mn

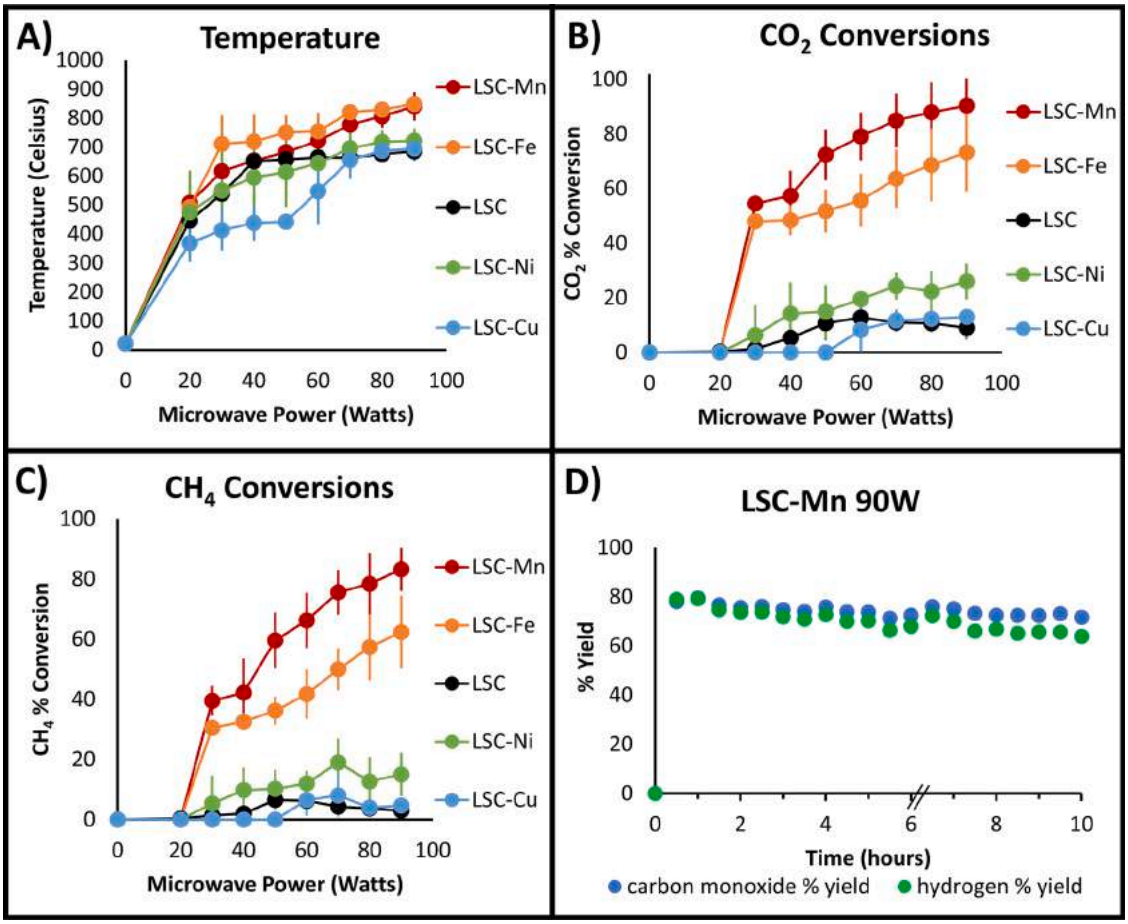


**Fig. 2.** Doped LSC-M performance versus applied MW wattage. (A) Apparent, pyrometer measured catalyst temperature versus applied microwave power. (B) Steady-state single-pass $CO_2$ and (C) $CH_4$ conversion versus microwave power. All runs were performed at least in triplicate with error bars showing one standard deviation. (D) Gas chromatograph measured CO and $H_2$ % yields at a constant 90 W. The system was shut down at the 6-h mark and resumed the following day (indicated with broken x-axis symbol).

converted 90 ± 10 % of $CO_2$ and 83 ± 7% of $CH_4$ while producing $H_2$ and CO at a 0.93:1 ratio at 90 W applied MW power. This represents a roughly 9-fold improvement in conversions compared with pure LSC. All catalyst runs were at least in triplicate, and the data for LSC-Mn represents 5 separate runs with 4 independently synthesized batches. LSC-Mn also showed drastically improved stability compared with pure LSC and demonstrated over 10 h of sustained MW-DRM (Fig. 2D). Importantly, the system was powered down overnight after six hours of runtime and kept under 4% $CO_2$ and 4% $CH_4$ gas, and we did not observe any obvious decrease in catalytic activity upon resuming MW irradiation. This ability to shut down and resume indicates clear potential for on-demand chemical production using excess or intermittent renewable electricity without the long cooldown and warm up periods needed for high temperature thermal reactors. However, a gradual decrease in product formation was observed over 10 h of operation. $CO_2$ conversions dropped at a slower rate, suggesting $CH_4$ active sites were lost at a faster rate than $CO_2$ active sites due to potential coking or metal site sintering. We found that microwaving the catalyst under pure $CO_2$ regenerated performance to that of a fresher catalyst (Fig. S5), which provides a convenient method for reactivating catalysts.

### 3.3. Post reaction characterization

Post-reaction XRD and SEM-EDX were used to analyze structural changes and quantify the degree of phase separation after the MW-DRM runs (Fig. 3). LSC-Cu showed the most dramatic phase separation as metallic Cu visibly leeched out of the powder and SEM-EDX showed micrometer-sized Cu (yellow) particles and surface enrichment of Sr (red). LSC-Ni, LSC, and LSC-Fe all exhibited large >300 nm cobalt particles (blue) and extensive La (green) and Sr (red) phase separations, consistent with the problematic Sr phase separation that has been reported for LSC surfaces [41]. On the other hand, LSC-Mn showed much less phase separation. Post-reaction XRD was used to observe the degree of phase separation for each catalyst. As seen in Fig. 3F and G, LSC-Mn maintained the most $A_2BO_4$ phase with the smallest $Co_{fcc}$ and $La_2O_3$ features after running the MW-DRM reaction from 20−90 W while LSC-Cu had the least remaining $A_2BO_4$.

STEM-EDX (Fig. 4) characterization of post reaction LSC-Mn revealed the formation of exsolved Co nanoparticles with a diameter distribution centered around 100 nm. The catalyst surface appeared generally well mixed with Co, Mn, La, and Sr, which is consistent with SEM results in Fig. 3 and indicates retention of the perovskitic phase. STEM-EDX of unsubstituted LSC (Fig. S6) largely replicated SEM results in Fig. 3 and showed the formation of ~350 nm cobalt particles and surface areas that were severely depleted of cobalt and predominantly composed of $La_2O_3$ or Sr oxides.

### 3.4. Bader charge analysis

DFT calculations and Bader charge analyses were performed to investigate dopant-induced modifications to the LSC electronic structure. As expected, less electronegative dopant atoms (e.g. Mn) redistributed electron density towards oxygen and resulted in a larger magnitude of the oxygen charge (i.e. more ionic bonding). The LSC-M oxygen Bader charge corresponded linearly with perovskite reducibility as determined from temperature programmed reduction (TPR) in 10 % $H_2$ (Fig. 5 A, S7, S8), and inclusion of less electronegative dopants increased the LSC-M reduction temperature. This result confirms that less electronegative dopants increased LSC-M oxophilicity and produced a perovskite that is better able to retain its oxide structure under reducing conditions. Worth noting, an increase in Mn content from 10 % was found to further increase the reduction temperature of LSC-Mn perovskites, allowing additional control over the oxophilicity of the catalyst. However, additional Mn did not significantly affect catalyst performance in our reaction conditions (S9).

### 3.5. Oxygen k-edge X-ray absorption

We directly measured the electronic structure changes in LSC-M using oxygen K-edge X-ray absorption spectroscopy (Fig. 5B). The pre-edge doublet structure (peaks A and B) around 530 eV are attributed to excitation from the O 1s ground state to the hybridized $Co_{3d}$-$O_{2p}$ state,

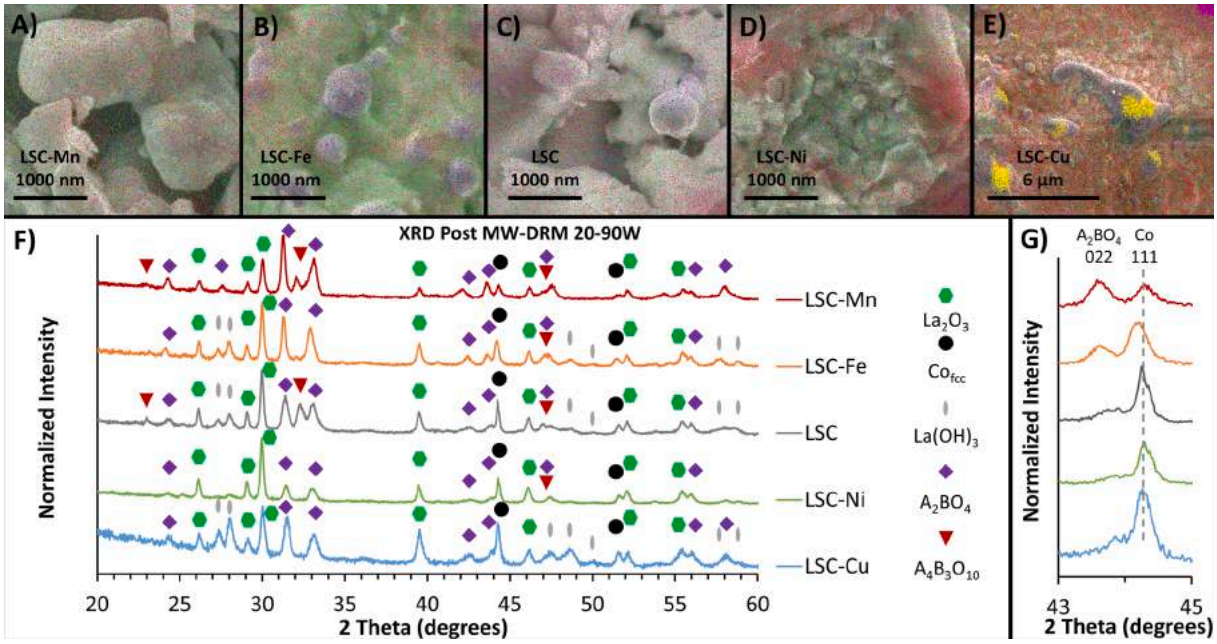


**Fig. 3.** LSC-M structure changes after MW-DRM. (A-E) SEM-EDX images of post-reaction LSC-Mn, LSC-Fe, LSC, LSC-Ni, and LSC-Cu (respectively) catalysts after the MW-DRM studies shown in Fig. 2. For all the images: blue = cobalt, green = lanthanum, red = strontium, and yellow = dopant element. The LSC-Cu sample is shown at lower magnification to capture the large-scale phase separation and micron-sized Cu particles. (F) Corresponding XRD patterns of LSC-M catalysts after MW-DRM experiments. Note that $A_2BO_4$ and $A_4B_3O_{10}$ are both perovskitic Ruddlesden-Popper ($A_{n+1}B_nO_{3n+1}$) phases. (G) Magnified XRD patterns showing increased retention of the Ruddlesden-Popper $A_2BO_4$ phase and smaller amount of Co with LSC-Fe and LSC-Mn.

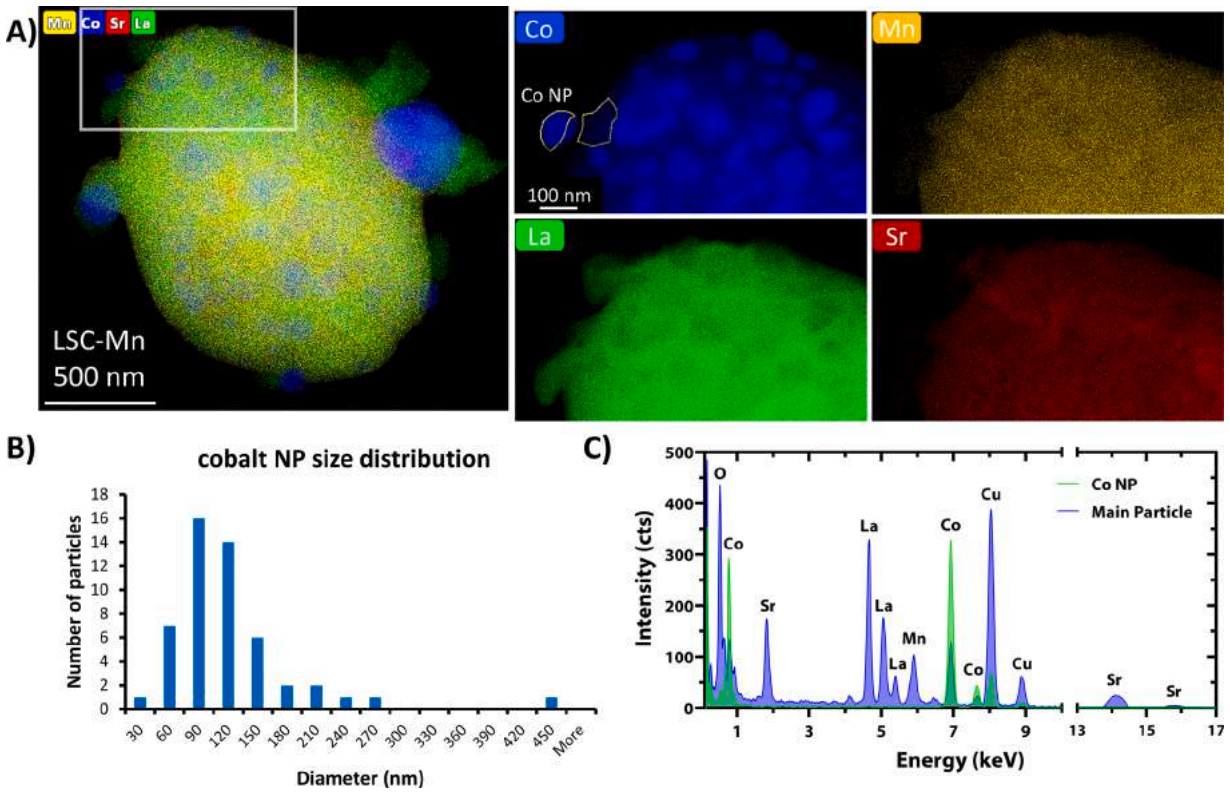


**Fig. 4.** STEM-EDX of LSC-Mn after MW-DRM. (A) STEM-EDX image of LSC-Mn particle after use in the MW-DRM studies shown in Fig. 2; inset images show individual element maps at higher magnification. (B) Cobalt nanoparticle histogram (n = 51 particles). (C) EDX spectra of the cobalt nanoparticle (Co NP = green spectrum) highlighted above along with the adjacent area of the main particle (blue spectrum). The Cu signal originated from the TEM grid.

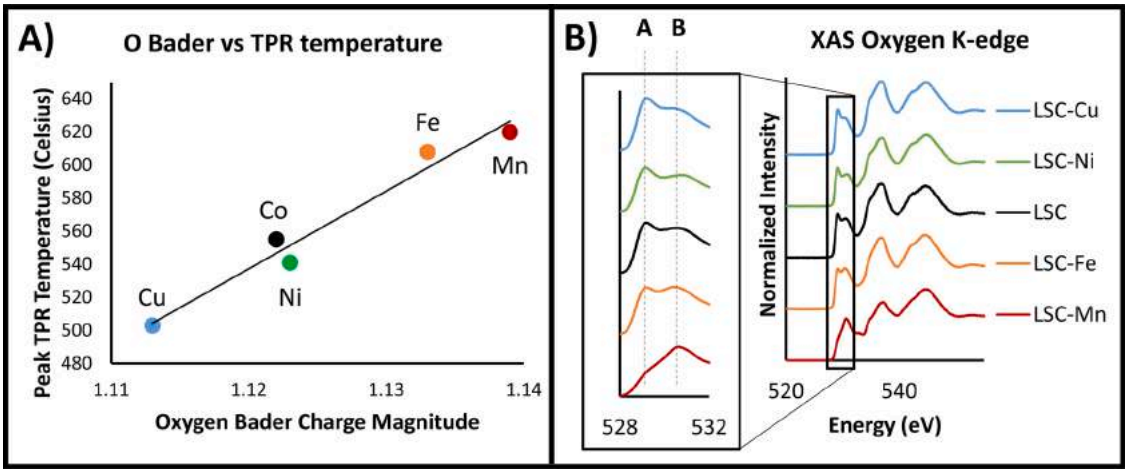


**Fig. 5.** Dopant effect on LSC oxygen bonding. (A) Peak $H_2$ TPR temperature for LSC-M samples versus calculated Bader charge on the perovskite oxygen atoms. (B) Oxygen K-edge X-ray absorption spectra of the as-prepared LSC-M catalysts.

meaning that completely ionic oxides are expected to not exhibit these O-K pre-edge structures at around 530 eV [42–44]. As shown in Fig. 5b, all five LSC based catalysts display peaks around 530 eV and show varying degrees of Co-O covalency. The presence of feature A has been experimentally found to indicate oxygen vacancies in LSC perovskites [45]. As the pre-edge feature A was found to be nearly absent from LSC-Mn and increase across the period, this suggests that the addition of Mn and Fe increased the oxophilicity of the perovskite and decreased the amount of oxygen vacancies in the material. Conversely, the addition of Ni and Cu decreased the oxophilicity leading to a less fully oxidized material even at room temperature. Taken together, the stability trends from TPR, electronic structure calculations, and XAS results indicate that the key to improving catalyst stability is an oxophilic and difficult to reduce perovskite catalyst.

### 3.6. *In situ XRD of LSC-Mn*

We conducted in situ s-XRD of the LSC-Mn catalyst during thermal DRM to study the real-time phase transformation and determine the active catalyst structure. In situ s-XRD experiments were conducted using a quartz microcapillary packed bed reactor with in-line mass spectrometry. Control experiments confirmed both thermal and MW-DRM produced consistent products and structural changes (Fig. S10), although somewhat higher thermal reactor temperatures were required

to initiate DRM product formation (>800 °C) compared with the optically-measured apparent temperatures recorded during MW-DRM reactions (600−700 °C). This observation is likely due to local hot-spots that form at the center of the catalyst plug below the top surface as has been observed previously in microwave systems [39], but the underlying reaction and catalyst structural changes remain the same during both thermal and MW-DRM. It is worth noting that we observed a tighter particle size distribution after thermal DRM (70 ± 20 nm), likely due to the absence of localized hot-spots associated with MW heating (S11).

Fig. 6 presents in situ s-XRD patterns of LSC-Mn during thermal DRM. In situ s-XRD trends largely mimicked those observed for ex situ MW-DRM in Fig. 1B during the initial activation region. LSC-Mn underwent a first phase transition starting at ~720 °C where the perovskite $ABO_3$ structure changed into to BO (CoO) and $A_2BO_4$ ($La_xSr_{2-x}CoO_4$). CoO was then reduced into metallic Co at 820−840 °C. Fig. 6C highlights the emergence of the Co (002) peak, which coincides with the second reduction step in Fig. 1A. The formation of metallic Co was strongly coupled with the loss of the CoO periclase phase, but the Ruddlesden-Popper $La_xSr_{2-x}CoO_4$ remained stable. This result strongly suggests that the metallic Co formed through CoO reduction, rather than continued exsolvation of Co from $La_xSr_{2-x}CoO_4$. Online gas analysis identified the onset of $H_2$ and CO production coincided with the formation of metallic Co at 820 °C (Fig. 6D). This result strongly identifies the newly formed Co metal sites as key reaction centers in the DRM reaction. Small $SrCO_3$ features were also observed at temperatures above 760 °C (Fig. 6B), but this feature gradually decreased above ~860 °C as $SrCO_3$ was likely reincorporated back into the $La_xSr_{2-x}CoO_4$ phase. This observation explains why widespread $SrCO_3$ deposits were not visible on the LSC-Mn surface post reaction (Fig. 3A), and it also suggests that improved $La_xSr_{2-x}CoO_4$ phase stability in LSC-Mn prevented $SrCO_3$ from poisoning the catalyst surface.

Previous thermal studies on La perovskites have suggested that fully phase separated metallic particles on $La_2O_3$ are the active catalyst for the dry reforming reaction with $CO_2$ activation occurring through a $La_2O_2CO_3$ intermediate that forms on $La_2O_3$ [16,46–48]. This structure corresponds to the third reduction step in Fig. 1A. Notably, our in situ s-XRD results did not identify complete phase separation of LSC-Mn into metallic Co and $La_2O_3$ in our active catalyst at the maximum experimental temperature (900 °C). Rather, our experimental results identify that metallic Co formation (but not $La_2O_3$) is crucial for the DRM activity of the LSC-Mn catalyst. This means that the catalyst must readily reduce through the first and second reduction shown in in Fig. 1a but should not over-reduce to phase separated metals and oxides for ideal MW-DRM activity. Finally, we tracked the regeneration of the initial LSC-Mn catalyst structure after thermal DRM by heating in 20 % $O_2$ and observed that Co was reabsorbed as the catalyst re-oxidized and ultimately reformed the initial perovskite structure at 880 °C (Fig. S13). This result further confirms the catalyst's ability to be regenerated under oxidizing conditions and provides a simple way to remove coke formations.

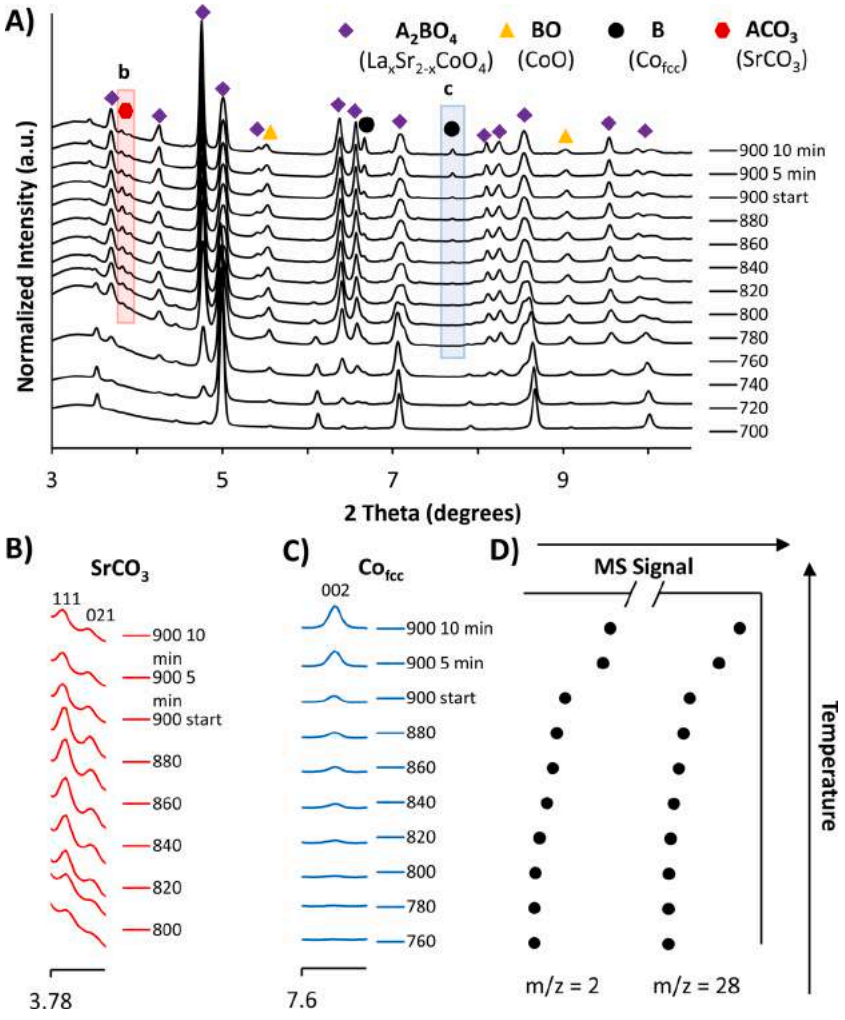


**Fig. 6.** In situ s-XRD of LSC-Mn during DRM. (A) In situ s-XRD patterns of LSC-Mn as it became active for the DRM reaction in the presence of $CO_2$ and $CH_4$. Simultaneous mass spectrometry data shown in Fig S12. (B) Magnification of area shown above showing strontium carbonate beginning to separate before reincorporating during DRM. (C) Magnified area of above patterns showing the temperature when Co separates and (D) simultaneously measured $H_2$ ($m/z$ = 2) and CO ($m/z$ = 28) mass spectrometer signals at the same temperatures.

### 3.7. Performance of LSC-Mn under pure gases

LSC-Mn was found to be able to achieve ~80 % or higher single-pass conversions of undiluted (50:50) $CO_2$:$CH_4$ gas mixtures up to a space velocity of ~24 $Lg^{-1}hr^{-1}$ (Figure S14). Higher space velocities generally required higher microwave powers with peak conversion efficiency in our tests at ~12 $Lg^{-1}hr^{-1}$. Running at 10 $Lg^{-1}hr^{-1}$ and 140 W, we found that LSC-Mn readily could sustain >80 % conversion of undiluted gas for over 3 h with a 0.94:1 $H_2$:CO ratio (Fig. 7). In comparison, Gangurde et al. [21] demonstrated similar performance with $Ru/SrTiO_3$ microwave catalysts that required 150 W to sustain conversion at 9 $Lg^{-1}hr^{-1}$. However, the LSC-Mn catalyst reported here eliminates the need for platinum group metals. Ongoing efforts will optimize catalyst preparation (monolith, pellet, etc.) and reactor design for high flow operation and scaling studies.

## 4. Conclusions

We have demonstrated the use of LSC-M as catalysts for MW-DRM applications. Our results identify important design principles for MW-DRM catalysts and suggest that the active sites on LSC-Mn catalysts are cobalt particles on a Ruddleden-Popper ($La_xSr_{2-x}CoO_4$) support that form after the initial perovskite has partially reduced during the initial combustion of methane with lattice oxygen. Effective microwave dry reforming LSC based catalysts must be reducible enough to exsolve metal active sites at the surface yet resist over-reduction and complete phase separation under reaction conditions. The oxophilicity of the B site element was identified as a key parameter for this balancing act. Incorporating Mn atoms into the perovskite lattice reinforced the B—O— B bonds and made the structure less susceptible to oxide over-reduction, structural rearrangement, and phase separations. This had the dual benefits to MW-DRM performance of 1) extending the temperature range at which the microwave absorbing perovskitic phase was stable, and 2) sustaining small, catalytically active cobalt nanoparticles on a stable perovskitic oxide support by preventing complete phase segregation. In-situ reaction of 20 % oxygen showed this process to be reversible with the metallic cobalt phases reabsorbed back into the initial $ABO_3$ perovskite structure. Our results show that over-reduction can be controlled to a large extent through catalyst composition, and that regeneration from over reduction, carbon, and sintering are accomplished simultaneously by microwaving or heating in oxidative conditions, which returns the sample to that of the original perovskite, without requiring a separate regeneration unit. Tests with undiluted (50:50 $CO_2$:$CH_4$) also show LSC-Mn can achieve at least 80 % conversions at space velocities up to ~24 $Lg^{-1}hr^{-1}$ and can readily sustain conversions at 10 $Lg^{-1}hr^{-1}$ for over 3 h at 140 W. Ongoing efforts will optimize catalyst structure (pellet, monolith, etc.), reactor parameterization (higher flow rates, thermal insulation, etc.) for scaling studies to further evaluate MW-DRM for on-demand syngas production from captured $CO_2$ and $CH_4$.

## Funding

This work was performed in support of the US Department of Energy's Fossil Energy Crosscutting Technology Research Program. The Research was executed through the NETL Research and Innovation Center's $CO_2$ Utilization Technologies. Research performed by Leidos Research Support Team staff was conducted under the RSS contract 89243318CFE000003. This research used the 23-ID-2 (IOS) beamline of the National Synchrotron Light Source II, a U.S. Department of Energy (DOE) Office of Science User Facility operated for the DOE Office of Science by Brookhaven National Laboratory under Contract No. DE-SC0012704. This research used Beamline 17-BM of the Advanced Photon Source, a U.S. Department of Energy (DOE) Office of Science User Facility operated for the DOE Office of Science by Argonne National Laboratory under Contract No. DE-AC02−06CH11357.

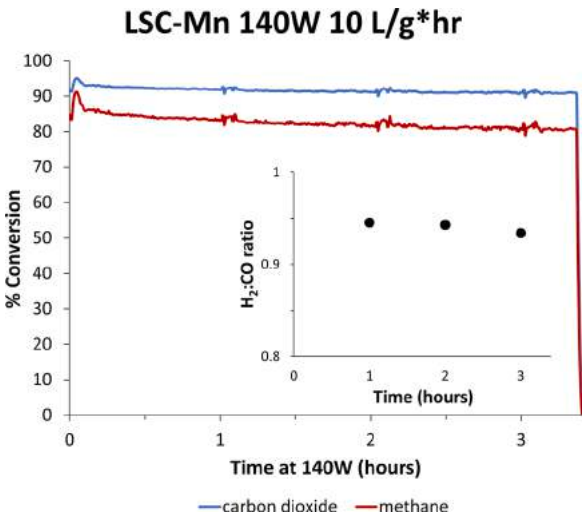


**Fig. 7.** LSC-Mn DRM performance using undiluted gases. Mass spectrometry measured percent conversions of $CO_2$ and $CH_4$ versus time at 140 W and 100 sccm using 0.6 g of LSC-Mn. (Inset) GC determined $H_2$:CO product ratios from gas sampled hourly.



## Author contributions

CMM performed the microwave studies, SEM characterization, and analyses. EJP synthesized the perovskites and ran XRD. CMM, EJP, and T-D N-P also performed the synchrotron experiments with the assistance of IW, AH, and WX. DFT and Bader charge calculations were performed by DA and DNT. DRK provided technical guidance and was responsible for the studies performed. All authors contributed to the preparation of the manuscript.

## CRediT authorship contribution statement

**Chris M. Marin:** Conceptualization, Methodology, Investigation, Formal analysis, Resources, Writing - original draft. **Eric J. Popczun:** Investigation, Resources. **Thuy-Duong Nguyen-Phan:** Investigation, Resources. **De Nyago Tafen:** Formal analysis, Resources, Investigation. **Dominic Alfonso:** Formal analysis, Resources. **Iradwikanari Waluyo:** Resources, Investigation. **Adrian Hunt:** Resources, Investigation. **Douglas R. Kauffman:** Conceptualization, Supervision, Project administration, Funding acquisition, Writing - review & editing.

## Declaration of Competing Interest

A US patent application has been filed based on this published research.

## Acknowledgments

General: We thank Dr. Brett Howard and Dr. Sittichai Natesakhawat for assistance with XRD, SEM, TPR, thermal DRM experiments, and for helpful discussions. Additionally, we thank Dr. Junseok Lee and Dr. Xingyi Deng for helpful discussions and manuscript feedback. We also thank Dr. Stephen House at the University of Pittsburgh for his TEM analysis. Finally, we thank Dr Wenqian Xu at Argonne National Laboratory beamline 17-BM for assisting with collecting the s-XRD data.

## Appendix A. Supplementary data

Supplementary material related to this article can be found, in the online version, at doi:https://doi.org/10.1016/j.apcatb.2020.119711.

## References

[1] S. Chu, N. Liu, The path towards sustainable energy, Nat. Mater. 16 (2017) 16–22.
[2] R.A. Alvarez, D. Zavala-Araiza, D.R. Lyon, D.T. Allen, Z.R. Barkley, A.R. Brandt, K. J. Davis, S.C. Herndon, D.J. Jacob, A. Karion, E.A. Kort, B.K. Lamb, T. Lauvaux, J. D. Maasakkers, A.J. Marchese, M. Omara, S.W. Pacala, J. Peischl, A.L. Robinson, P. B. Shepson, C. Sweeney, A. Townsend-Small, S.C. Wofsy, S.P. Hamburg, Assessment of methane emissions from the U.S. oil and gas supply chain, Science 361 (2018) 186–188.
[3] Y. Konno, T. Fujii, A. Sato, K. Akamine, M. Naiki, Y. Masuda, K. Yamamoto, J. Nagao, Key findings of the world's first offshore methane hydrate production test off the coast of Japan: toward future commercial production, Energy Fuels 31 (2017) 2607–2616.
[4] N.J. Gunsalus, A. Koppaka, S.H. Park, S.M. Bischof, B.G. Hashiguchi, R.A. Periana, Homogeneous functionalization of methane, Chem. Rev. 117 (2017) 8521–8573.
[5] S. Abelló, D. Montané, Exploring iron-based multifunctional catalysts for fischer-tropsch synthesis: a review, ChemSusChem 4 (2011) 1538–1556.
[6] M.K. Nikoo, N.A.S. Amin, Thermodynamic analysis of carbon dioxide reforming of methane in view of solid carbon formation, Fuel Process. Technol. 92 (2011) 678–691.
[7] R. Béchara, H. Hamadeh, O. Mirgaux, F. Patisson, Optimization of the Iron ore direct reduction process through multiscale process modeling, Materials 11 (2018).
[8] K. Wittich, M. Krämer, N. Bottke, S.A. Schunk, Catalytic dry reforming of methane: insights from model systems, ChemCatChem 12 (2020) 2130–2147.
[9] S. Hamzehlouia, S.A. Jaffer, J. Chaouki, Microwave heating-assisted catalytic dry reforming of methane to syngas, Sci. Rep. 8 (2018).
[10] B. Fidalgo, J.A. Menéndez, Syngas production by CO2 reforming of CH4 under microwave heating - Challenges and opportunity, in: A. Indarto, J. Palguandi (Eds.), Syngas: Production, Applications and Environmental Impact, Nova Science Publishers, Inc., 2013, pp. 121–149.
[11] S.T. Wismann, J.S. Engbæk, S.B. Vendelbo, F.B. Bendixen, W.L. Eriksen, K. Aasberg-Petersen, C. Frandsen, I. Chorkendorff, P.M. Mortensen, Electrified methane reforming: a compact approach to greener industrial hydrogen production, Science 364 (2019) 756–759.
[12] B. Fidalgo, A. Domínguez, J.J. Pis, J.A. Menéndez, Microwave-assisted dry reforming of methane, Int. J. Hydrogen Energy 33 (2008) 4337–4344.
[13] M. Usman, W.M.A.W. Daud, H.F. Abbas, Dry reforming of methane: influence of process parameters-A review, Renewable Sustainable Energy Rev. 45 (2015) 710–744.
[14] S.M. Kim, P.M. Abdala, T. Margossian, D. Hosseini, L. Foppa, A. Armutlulu, W. Beek, A. Comas-Vives, C. Copéret, C. Müller, Cooperativity and dynamics increase the performance of NiFe dry reforming catalysts, J. Am. Chem. Soc. 139 (2017) 1937–1949.
[15] I.V. Yentekakis, G. Goula, M. Hatzisymeon, I. Betsi-Argyropoulou, G. Botzolaki, K. Kousi, D.I. Kondarides, M.J. Taylor, C.M.A. Parlett, A. Osatiashtiani, G. Kyriakou, J.P. Holgado, R.M. Lambert, Effect of support oxygen storage capacity on the catalytic performance of Rh nanoparticles for $CO_2$ reforming of methane, Appl. Catal. B 243 (2019) 490–501.
[16] K. Li, C. Pei, X. Li, S. Chen, X. Zhang, R. Liu, J. Gong, Dry reforming of methane over $La_2O_2CO_3$-modified Ni/Al2O3 catalysts with moderate metal support interaction, Appl. Catal. B 264 (2020), 118448.
[17] S. Chen, J. Zaffran, B. Yang, Dry reforming of methane over the cobalt catalyst: theoretical insights into the reaction kinetics and mechanism for catalyst deactivation, Appl. Catal. B 270 (2020), 118859.
[18] Z. Bian, Z. Wang, B. Jiang, P. Hongmanorom, W. Zhong, S. Kawi, A review on perovskite catalysts for reforming of methane to hydrogen production, Renewable Sustainable Energy Rev. 134 (2020), 110291.
[19] X. Zhang, C.S.-M. Lee, D.M.P. Mingos, D.O. Hayward, Carbon dioxide reforming of methane with Pt catalysts using microwave dielectric heating, Catal. Lett. 88 (2003) 129–139.
[20] H.M. Nguyen, G.H. Pham, R. Ran, R. Vagnoni, V. Pareek, S. Liu, Dry reforming of methane over Co-Mo/$Al_2O_3$ catalyst under low microwave power irradiation, Catal. Sci. Technol. (2018).
[21] L.S. Gangurde, G.S.J. Sturm, M.J. Valero-Romero, R. Mallada, J. Satamaria, A. I. Stankiewicz, G.D. Stefanidis, Synthesis, characterization, and application of ruthenium-doped $SrTiO_3$ perovskite catalysts for microwave-assisted methane dry reforming, Chem. Eng. Process. Process. Intensif. 127 (2018) 178–190.
[22] H. Kozuka, K. Ohbayashi, K. Koumoto, Electronic conduction in La-based perovskite-type oxides, Sci. Technol. Adv. Mater. 16 (2015).
[23] Y. Yu, H. Luo, D. Cetin, X. Lin, K. Ludwig, U. Pal, S. Gopalan, S. Basu, Effect of atmospheric $CO_2$ on surface segregation and phase formation in $La_{0.6}Sr_{0.4}Co_{0.2}Fe_{0.8}O_{3-}\delta$ thin films, Appl. Surf. Sci. 323 (2014) 71–77.
[24] Y. Gao, Z. Lu, T.L. You, J. Wang, L. Xie, J. He, F. Ciucci, Energetics of nanoparticle exsolution from perovskite oxides, J. Phys. Chem. Lett. 9 (2018) 3772–3778.
[25] K.-Y. Lai, A. Manthiram, Self-regenerating Co-Fe nanoparticles on perovskite oxides as a hydrocarbon fuel oxidation catalyst in solid oxide fuel cells, Chem. Mater. 30 (2018) 2515–2525.
[26] E.P. Komarela, I. Komissarov, B.A. Rosen, Effect of Fe and Mn substitution in $LaNiO_3$ on exsolution, activity, and stability for methane dry reforming, Catalysts 10 (2020) 14.
[27] X. Song, X. Dong, S. Yin, M. Wang, M. Li, H. Wang, Effects of Fe partial substitution of $La_2NiO_4/LaNiO_3$ catalyst precursors prepared by wet impregnation method for the dry reforming of methane, Appl. Catal. A Gen. 526 (2016) 132–138.
[28] J.W. Lekse, S. Natesakhawat, D. Alfonso, C. Matranga, An experimental and computational investigation of the oxygen storage properties of $BaLnFe2O_{5+\delta}$ and $BaLnCo2O_{5+\delta}$ (Ln ¼ La, Y) perovskites, J. Mater. Chem. A 2 (2014) 2397–2404.
[29] B.H. Toby, R.B.V. Dreele, GSAS-II: the genesis of a modern open-source all purpose crystallography software package, J. Appl. Crystallogr. 46 (2013) 544–549.
[30] B. Ravel, M. Newville, ATHENA, ARTEMIS, HEPHAESTUS: data analysis for X-ray absorption spectroscopy using IFEFFIT, J. Synchrotron Radiat. 12 (2005) 537–541.
[31] G. Kresse, J. Hafner, Norm-conserving and ultrasoft pseudopotentials for first-row and transition elements, J. Phys. Condens. Matter 6 (1994).
[32] J.P. Perdew, K. Burke, M. Ernzerhof, Generalized gradient approximation made simple, Phys. Rev. Lett. 77 (1996).
[33] L. Wang, T. Maxisch, G. Ceder, Oxidation energies of transition metal oxides within the GGA+U framework, Phys. Rev. B 73 (2006).
[34] A.N. Petrov, V.A. Cherepanov, A.Y. Zuev, Thermodynamics, defect structure, and charge transfer in doped lanthanum cobaltites: an overview, J. Solid State Electrochem. 10 (2006) 517–537.
[35] F. Riza, C. Ftikos, Influence of A- and B-site doping on the properties of the system $La_2CoO_{4\pm}\delta$, J. Eur. Ceram. Soc. 27 (2007) 571–573.
[36] N. Kamiuchi, K. Sun, R. Aso, M. Tane, T. Tamaoka, H. Yoshida, S. Takeda, Self-activated surface dynamics in gold catalysts under reaction environments, Nat. Commun. 9 (2018).
[37] K.-i. Tanaka, Catalysts working by self-activation, Appl. Catal. A Gen. 188 (1999) 37–52.
[38] K.P. Kepp, A quantitative scale of oxophilicity and thiophilicity, Inorg. Chem. 55 (2016) 9461–9470.
[39] L.S. Gangurde, G.S.J. Sturm, T.J. Devadiga, A.I. Stankiewicz, G.D. Stefanidis, Complexity and challenges in noncontact high temperature measurements in microwave-assisted catalytic reactors, Ind. Eng. Chem. Res. 56 (2017) 13379–13391.
[40] H. Wang, X. Dong, T. Zhao, H. Yu, M. Li, Dry reforming of methane over bimetallic Ni-Co catalyst prepared from $La(Co_xNi_{1-x})_{0.5}Fe_{0.5}O_3$ perovskite precursor: catalytic activity and coking resistance, Appl. Catal. B 245 (2019) 302–313.
[41] J. Ovenstone, J.S. White, S.T. Misture, Phase transitions and phase decomposition of $La_{1-x}Sr_xCoO_{3-\delta}$ in low oxygen partial pressures, J. Power Sources 181 (2008) 56–61.
[42] Y. Orikasa, T. Ina, T. Nakao, A. Mineshige, K. Amezawa, M. Oishi, H. Arai, Z. Ogumi, Y. Uchimoto, X-ray Absorption Spectroscopic Study on $La_{0.6}Sr_{0.4}CoO_{3-}\delta$ cathode materials related with oxygen vacancy formation, J. Phys. Chem. C 115 (2011) 16433–16438.
[43] L. Karvonen, M. Valkeapää, R.-S. Liu, J.-M. Chen, H. Yamauchi, M. Karppinen, O-K and Co-L XANES study on oxygen intercalation in perovskite SrCoO3-δ, Chem. Mater. 22 (2010) 70–76.
[44] J. Suntivich, W.T. Hong, Y.-L. Lee, J.M. Rondinelli, W. Yang, J.B. Goodenough, B. Dabrowski, J.W. Freeland, Y. Shao-Horn, Estimating hybridization of transition metal and oxygen states in perovskites from O K-edge X-ray absorption spectroscopy, J. Phys. Chem. C 118 (2014) 1856–1863.
[45] A.R. Moodenbaugh, B. Nielsen, S. Sambasivan, D.A. Fischer, T. Friessnegg, S. Aggarwal, R. Ramesh, R.L. Pfeffer, Hole-state density of $La_{1-x}Sr_xCoO_{3-\delta}(0\notin x\notin 0.5)$ across the insulator/metal phase boundary, Phys. Rev. B 61 (2000).
[46] R. Pereñíguez, V.M. González-DelaCruz, J.P. Holgado, A. Caballero, Synthesis and characterization of a $LaNiO_3$ perovskite as percursor for methane reforming reactions catalysts, Appl. Catal. B 93 (2010) 346–353.
[47] G. Valderrama, A. Kiennemann, M.R. Goldwasser, Dry reforming of $CH_4$ over solid solutions of $LaNi_{1-x}Co_xO_3$, Catal. Today 133-135 (2008) 142–148.
[48] G.S. Gallego, C. Batiot-Dupeyrat, J. Barrault, F. Mondragón, Dual active-site mechanism for dry methane reforming over Ni/$La_2O_3$ produced from $LaNiO_3$ perovskite, Ind. Eng. Chem. Res. 47 (2008) 9272–9278.
[49] A.N. Petrov, V.A. Cherepanov, A.Y. Zuyev, V.M. Zhukovsky, Thermodynamic stability of ternary oxides in Ln-M-O (Ln = La, Pr, Nd; m = Co, Ni, Cu) systems, J. Solid State Chem. 77 (1988) 1–14.